nature materials

LETTERS

PUBLISHED ONLINE: 16 OCTOBER 2017 | DOI: 10.1038/NMAT5008

Topological defects govern crack front motion and facet formation on broken surfaces

Itamar Kolvin, Gil Cohen and Jay Fineberg*

Cracks develop intricate patterns on the surfaces that they create. As faceted[1,2] fracture surfaces are commonly formed by slow tensile cracks in both crystalline and amorphous materials[3–5], facet formation and structure cannot reflect microscopic order. Although fracture mechanics predict that slow crack fronts should be straight and form mirror-like surfaces[6–9], facet-forming fronts propagate simultaneously within different planes separated by steps. Here we show that these steps are topological defects of crack fronts and that crack front separation into disconnected overlapping segments provides the condition for step stability. Real-time imaging of propagating crack fronts combined with surface measurements shows that crack dynamics are governed by localized steps that drift at a constant angle to the local front propagation direction while their increased dissipation couples to long-ranged elasticity to determine front shapes. We study how three-dimensional topology couples to two-dimensional fracture dynamics to provide a fundamental picture of how patterned surfaces are generated.

The surface patterns created by cracks are objects of fascination as well as practical utility[1], but the fundamental laws that govern their formation remain obscure. Classically, cracks are treated as two-dimensional (2D); fracture surfaces are reduced to a line ending at a singular point—the crack tip—where the two surfaces are created. Cracks will propagate when the energetic cost of breaking a unit surface area, the fracture energy Γ, is balanced by the energy flow to the singular crack tip, G; namely, $G=\Gamma$. Crack velocities are bounded by the Rayleigh surface wave speed, c_R. This framework[10] is very successful in predicting the dynamics of simple tensile cracks that produce structureless 'mirror' surfaces[11]. In three dimensions, the crack tip becomes a singular line, the crack front. The appearance of structure[1] and roughness[12] within fracture surfaces demonstrates the need for a 3D picture. Theory has, however, shown[6–9] that slow ($\ll c_R$) tensile (Mode I) crack fronts are stable to perturbations, although the addition of twist (Mode III) can destabilize crack fronts[13–17]. Surprisingly, experiments have shown that purely tensile cracks can spontaneously form structure. Faceted fracture surfaces appear in brittle materials ranging from crystalline silicon to amorphous polymers[1–5]. Here we examine how these non-trivial facets are created and how they couple to crack front dynamics.

Our experiments are performed in brittle polyacrylamide gels of dimensions $(x, y, z) = (54, 56, 4.6)$ mm under uniform tensile loading (Methods). In gels, crack speeds are reduced by two to three orders of magnitude[18] ($c_R \sim 5\ \mathrm{m\,s^{-1}}$) compared with hard brittle materials, enabling crack dynamics to be captured at unprecedented spatial and temporal resolution. We visualize crack fronts propagating along the x axis in real time by shining light through the transparent sample along the tensile y axis (Fig. 1a). The high curvature at the crack front deflects the light and forms a shadow image that is captured by a high-speed camera. We correlate crack front dynamics with the surface structure they generate via optical profilometer (Fig. 1b) measurements.

In Fig. 1c we present typical structures formed on fracture surfaces. These are highly sensitive to mean front velocities, v. At $v < 0.01c_R$, surfaces are either mirror-like or consist of two facets separated by a step-line. Once nucleated, step heights grow and stabilize at $40 \pm 10\,\mu$m. Steps then drift at an angle to the crack front. Nucleation is strongly facilitated near existing steps and sample boundaries. As crack velocities increase, step nucleation becomes increasingly frequent, leading to intersections and mergers of step-lines and increased velocity fluctuations. When $v \sim 0.05c_R$, microbranches, localized 10–100 μm cracks that branch off the main front[19], begin to appear and coexist with steps. For $v > 0.1c_R$, facets disappear altogether and successions of microbranches, or branch-lines, dominate the surface.

During the formation of facets, the in-plane (xz) profile of the crack front is curved. We observe ∼50 μm-wide strongly curved, 'cusp-like', regions at step locations from which long-range convex tails emanate, as shown in Fig. 2, where sequences of propagating fronts are superimposed on the fracture surface they created (see Supplementary Movies).

What determines step paths? Fracture surfaces yield a wide distribution of angles that step-lines form with the x axis. When step-lines exist simultaneously, their orientations can change during propagation (Fig. 3a). We define the step-line orientation as the angle θ relative to the local front normal, defined by the angle β relative to x. Whereas β varies between $-40°$ to $+40°$ due to both long-range curvature, induced by coexisting step-lines, and global front tilts, θ is narrowly distributed; $\theta = 43° \pm 5°$ (Fig. 3b). In addition, we find that local crack velocities along the front vary in proportion to the local front slope, $\partial x/\partial z$ (Fig. 3c).

What determines front shapes? When a crack is confined to a plane, fracture mechanics[20] tells us that at every point z along the crack front the local energy flux is equal to the local dissipation; $G(z) = \Gamma(z)$. Fracture mechanics also shows us how $G(z)$ is related to the crack front shape[21] (see Methods). On the other hand, steps increase fracture surface area, and hence locally increase $\Gamma(z)$. While steps are an inherently 3D entity, we will assume that the sole impact of steps on in-plane crack front dynamics and geometry is as a localized (since step widths are $<100\,\mu$m) in-plane perturbation to Γ. To capture both the localized and asymmetric character of the steps, we model the fracture energy as $\Gamma = \Gamma_0(1 + \delta A(z))$, where Γ_0 is the bare fracture energy[11,22] and $\Gamma_0\delta A$ is the contribution due to a step. The distribution $\delta A(z) = (2H/\pi W)(1 \pm \alpha(2z/W))/(1 + (4z^2/W^2))$ models the relative increase in surface area due to a step located at $z = 0$; W is its width, and the distribution is normalized so that $H = \int \delta A(z)\,\mathrm{d}z$ is the total surface area increase per unit crack length. Step asymmetry is quantified by $\pm\alpha$. Asymmetry is apparent in both the step out-of-plane profile, shown in Fig. 4a, and the in-plane

The Racah Institute of Physics, the Hebrew University of Jerusalem, Jerusalem 9190401, Israel. *e-mail: jay@mail.huji.ac.il

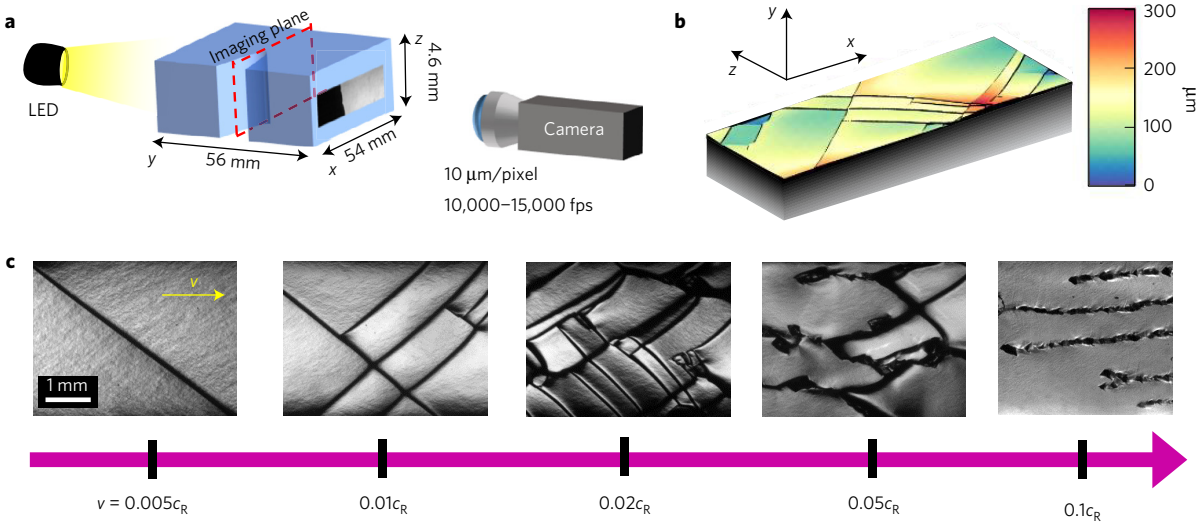

Figure 1 | Fracture surface patterns in brittle polyacrylamide gels. a, The experimental set-up. A rectangular gel slab is held in imposed tension along the *y* axis. The sample is illuminated by a collimated LED beam in the *y* direction. The light is deflected by the crack tip, producing shadow images of the propagating front that are captured by a fast camera. **b**, A profilometric surface scan performed after the experiment reveals a typical faceted surface. **c**, Images of typical fracture surfaces formed by cracks with increasing velocities. For $v < 0.01c_R$ fracture surfaces are either mirror-like, or contain a single step-line (first panel). As v is increased, step nucleation becomes more frequent (second and third panels) with step intersections forming cross-hatched patterns that are commonly observed[2–5] on fracture surfaces. At $v \sim 0.05c_R$ microbranches, which are localized kite-shaped structures, appear and coexist with step-lines (fourth panel). For $v \gtrsim 0.1c_R$ step-lines disappear altogether and microbranches appear in chains or branch-lines aligned parallel to the local front propagation direction (last panel). For our gels[11,18] $c_R = 5.2 \pm 0.2\,\mathrm{m\,s^{-1}}$.

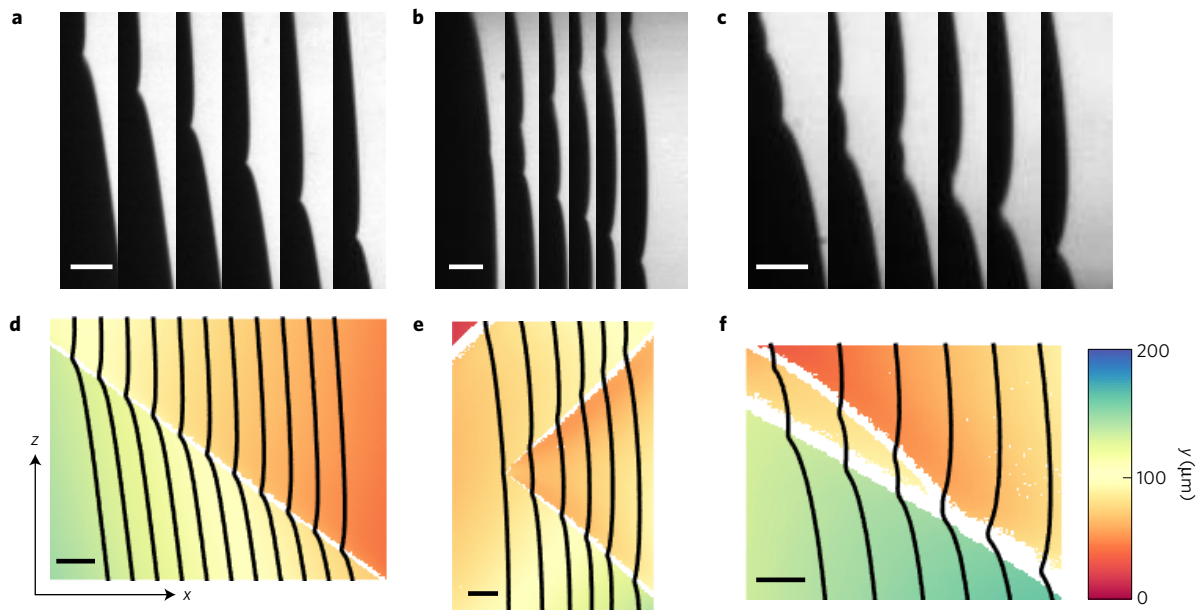

Figure 2 | Image sequences of facet-forming crack fronts and the resulting surface patterns. a–c, Sequences of crack fronts. **a**, A single step at $v = 0.005c_R$ displayed at 10 ms intervals. **b**, Two nucleating steps at $v \sim 0.01c_R$ displayed at 5 ms intervals. **c**, Merging step-lines at $v \sim 0.01c_R$ displayed at 5 ms intervals. **d–f**, Profilometric measurements of the fracture surfaces created by the fronts depicted in **a–c**, respectively. The fronts that formed them are overlaid in black. At steps, fronts are cusp-like with long-range curved tails. Scale bars are 200 μm long. White regions in the surface scan represent steep surface slopes.

front slopes $\partial x/\partial z$, as presented in Fig. 3c. The asymmetry is also apparent in profilometric measurements of step profiles (inset of Fig. 4d). Energy balance along a step-forming front dictates (see Methods) an in-plane profile given by[9] $x = x_0 + \delta x(z)$, where the step is located at $x = x_0$ and

$$\delta x(z) = cz + \frac{H}{\pi}\left[\frac{1}{2}\log\left(1+\frac{4z^2}{W^2}\right) \mp \alpha \arctan\left(\frac{2z}{W}\right)\right] \quad (1)$$

The solution $\delta x(z)$ also contains an overall tilt c. Equation (1) describes a locally concave profile with long-range logarithmic tails, as seen when interfacial crack fronts encounter a tough strip[23–25]. In Fig. 4b we present a typical example representative of more than 5,000 crack fronts (taken from 25 isolated step-lines). $W = 50^{+10}_{-3}$ μm and $\alpha = 0.24 \pm 0.08$ are approximately constant in our data (see Methods, Supplementary Fig. 1).

Importantly, the asymmetry sign $\pm\alpha$ always coincides with the step drift direction along the z axis; $+\alpha$ ($-\alpha$) when the step

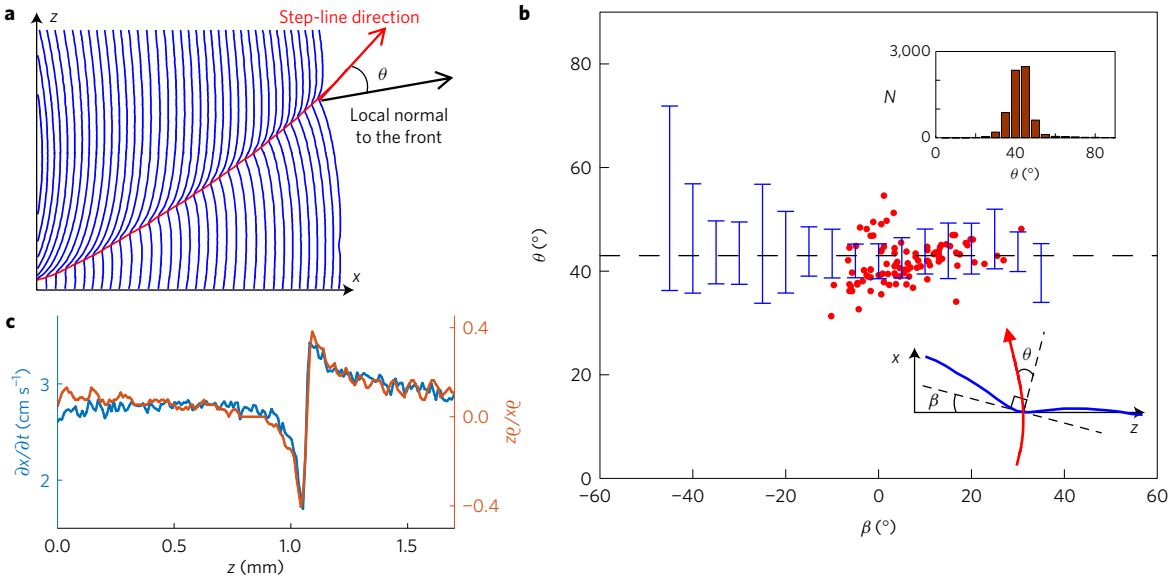

Figure 3 | Step-lines propagate at a constant angle to the local front normal in the crack frame. a, A sequence of crack fronts displayed at 0. 27 ms intervals (in blue) forms a step-line. The red line denotes cusp locations within the fronts associated with the step-line. As the step drifts along the front, its local orientation relative to the front changes, leading to step-line curvature. **b**, The angle $-40° < \beta < 40°$ depicts the local front orientation (bottom inset). The angle $\theta = 43° \pm 5°$ between the step-line and the local front direction remains constant. The blue bars show the range of θ in intervals of 5° in β, for more than 5,000 data points taken from 121 step-lines spanning $0.002c_R < v < 0.05c_R$. Top inset: distribution of all θ values. Red dots are θ values corresponding to **a**. **c**, At each instant, the local velocity $\partial x/\partial t$ varies in proportion to the local slope $\partial x/\partial z$—that is, the crack front contains a 'travelling wave' component $x(z,t) = az + vt + f(z-ut)$, where $u/v = \tan(\beta \pm \theta)$ (the sign of θ is positive (negative) for downward (upward) propagating steps).

drifts in the positive (negative) z direction. Examples are presented in Fig. 4c.

In Fig. 4d we compare values of H to the directly measured step heights h (Methods). As steady-state values of h are relatively constant ($h \sim 40\,\mu$m), a wide range of h was obtained by considering two cases of growth after nucleation and decay following step merging. As predicted by our model, the total surface area, as inferred from the in-plane profile, H, and directly measured out-of-plane step height, h, are proportional; $H \sim 1.4h$.

Why is $H > h$? A simple step of width w constitutes a surface area increase per unit crack length, $\sqrt{h^2 + w^2} - w$, which is always less than h. A closer look at the step structure reveals an additional hidden surface as noted previously[4,5] and shown in Fig. 4a. The lower part of Fig. 4a describes the front topology that produces this configuration. A step-forming front is composed of two disconnected simultaneously propagating branches. Their overlap is the hidden surface. The flat branch (denoted with a blue line) propagates slightly ahead of the curved branch (denoted in red). The curved branch terminates abruptly at the point where it meets the surface that was formed by the flat branch. As demonstrated in both Fig. 4a and d, the curved branch is steep near this point and becomes shallower as we move away from it. The total increase in step surface area must therefore include the hidden branch, explaining the relation $H \sim 1.4h$ since $w \sim h$, as profilometric data suggests (see Supplementary Fig. 2).

This non-trivial topology explains why steps are stable. Step stability can be understood by considering two limiting cases. Linearly perturbing a single continuous front both in-plane (δx) and out-of-plane (δy) generates two decoupled stress contributions[7,17,26,27]. δx induces tensile stresses that try to straighten the crack front, while δy generates shear stresses that tend to flatten it. For two overlapping fracture planes the picture changes[28,29]. When a crack splits into two branches, induced shear stresses cause the two branches to 'repel' each other; repulsion strength decreasing with branch separation. The repulsion is strong for small step heights and the two overlapping fracture surfaces are prevented from merging. On the other hand, the two branches of the crack front always retain coherence; macroscopically (Fig. 4b) the system behaves as a single in-plane crack subject to restoring tensile stresses. Plausibly, steps grow following nucleation due to branching repulsion and are later stabilized by the long-range restoring shear stresses that act along the front. The non-trivial topology of step-forming crack fronts, then, prevents them from decaying to a flat state; the crack front is composed of two disconnected entities and cannot be joined without changing the crack topology. This is the hallmark of a topological defect[4,5].

Why do steps drift along the front? Steps break reflection symmetry along the front ($\alpha \neq 0$ and $\theta \neq 0$). This suggests that stresses surrounding the step are distributed asymmetrically, which would lead to a bias in the step path. The value of θ, we believe, cannot be determined by the planar theory. The selection of θ must arise from the 3D configuration of the discontinuity at the step. Revealing the nature of the step requires a more rigorous discussion of the complex mixed-mode stresses that surround it.

Given the importance of three dimensionality to step stability, direction and dissipation, one might wonder why the planar theory works at all. Here, again, we draw an analogy from systems with topological defects. In these systems small-strain elasticity breaks down within a localized core region. In the case of an edge dislocation this core is the size of a few atomic distances. Outside of this region, elasticity remains valid, since strains are small. Similarly, outside of step regions, front deformations are still very much governed by in-plane elastic tension, although crack front branches lie in planes separated by tens of micrometres.

To conclude, our direct observations of facet-forming fronts enable us to quantitatively analyse otherwise hidden mechanisms. We have shown that we can quantitatively incorporate the effects of the complex 3D structure of a step into planar fracture mechanics by modelling a step as a localized, asymmetric energy sink. Combining the planar fracture mechanics description of the effects of energy dissipation at a step with the observed sharp selection of step-line paths explains how topological defects can govern crack front dynamics. Under quasistatic conditions, a drifting step causes a translation of the in-plane front profile along the z direction,

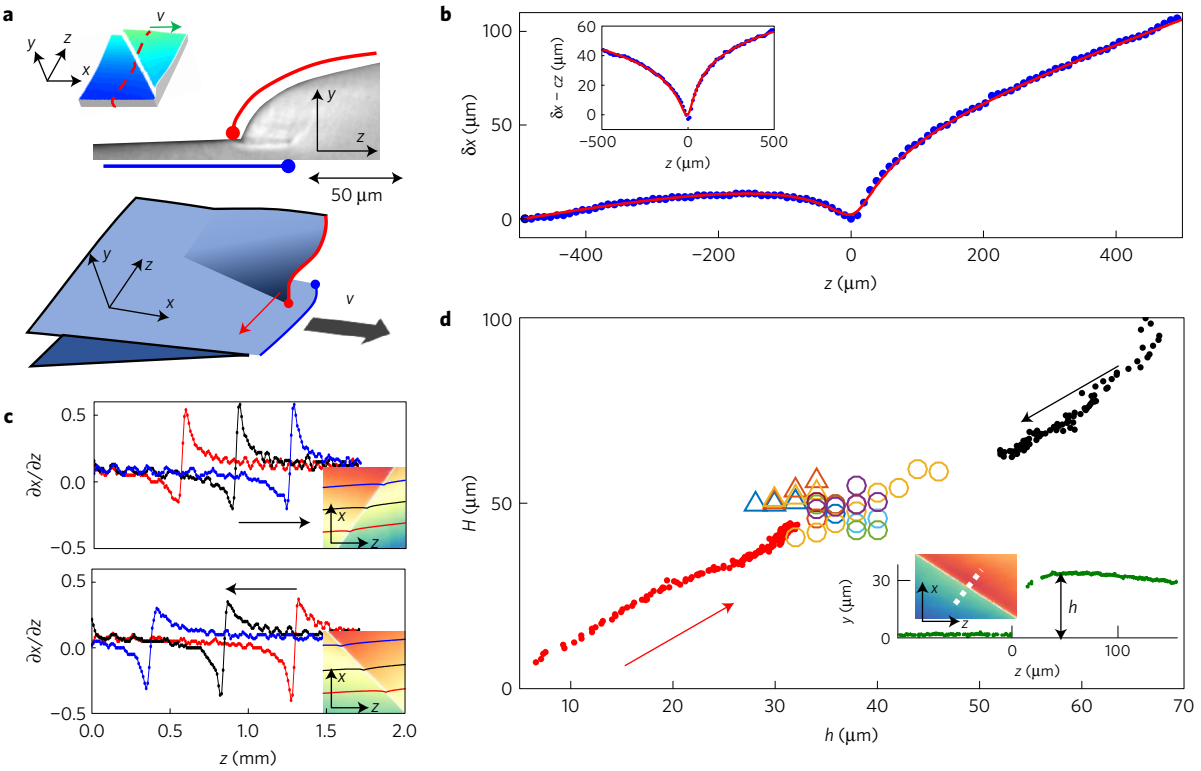

Figure 4 | Local dissipation at a step determines the long-range shape of the front. a, The formation of a step by a disconnected crack front. Top: a micrograph of the *yz* section of a typical step. The flat part of the step (blue) extends beneath the curved part (red) to form a hidden surface. Top inset: surface scan showing the cross-section orientation. Bottom: topology of a facet-forming crack front. One branch of the front (red) curves and connects to the flat surface that was formed by a second branch (blue). The curved branch (red) lags behind the flat branch (blue) while drifting along *z* (red arrow). **b**, A typical front profile around a step. Measurements (blue dots) are in excellent correspondence to the functional form $\delta x(z) = cz + (H/\pi)[1/2 \log(1 + (4z^2/W^2)) + \alpha \arctan(2z/W)]$ (red line) of width $W = 50\,\mu m$ and asymmetry $\alpha = 0.24$. (Inset) High-resolution comparison after removing the global tilt *cz*. **c**, Local front slopes reveal distinct asymmetry. The sign of $\pm\alpha$ always dictates step-line drift directions; drifts are positive (top) negative (bottom) for positive (negative) α. Insets: fracture surfaces formed by overlaid fronts. Colours as in main panel. **d**, In-plane front amplitudes *H* are proportional to out-of-plane step heights *h*; $H \sim 1.4h$. Red dots depict step-line rapid growth following the double nucleation event in Fig. 2b,e. Black dots depict step-line height decay following a merging event similar to Fig. 2c,f. Arrows depict growth (red) and decay (black). Triangles and circles depict step-lines near steady state, representing *H* values averaged over step heights *h* in 2 μm intervals. Different colours represent single step-lines (triangles) and step-lines coexisting with other surface structures (circles). Inset: a typical step profile *y*(*z*) along a section (dotted line) normal to the step-line presented.

enslaving the local velocities $\partial x/\partial t$ to front geometry, $\partial x/\partial z$, as shown in Fig. 3c.

Our results highlight a number of observations that may aid in the development of a fundamental theory of 3D crack front dynamics. The front asymmetry governs the sense of step drift and may be quantitatively described by a first-principles derivation of the 3D disconnected front configuration that produces a step. Although local front and step-line directions vary over a wide range of orientations (between 0° to 90° in our system), they form a sharply selected angle θ between them. θ should coincide with the mysterious 'magic angles' reported to emerge from fracture surface roughness[5], and the selection must result from a 3D fracture analysis where mode mixity should be relevant[17,27]. Step nucleation, growth and stability are all 3D effects and could involve nonlinear elasticity[5,14,30].

Methods

Methods, including statements of data availability and any associated accession codes and references, are available in the online version of this paper.

Received 12 February 2017; accepted 14 September 2017; published online 16 October 2017

References

1. Lawn, B. R. *Fracture of Brittle Solids* 2nd edn (Cambridge Univ. Press, 1993).
2. Kermode, J. R. *et al*. Low-speed fracture instabilities in a brittle crystal. *Nature* **455,** U1224–U1241 (2008).
3. Gent, A. N. & Pulford, C. T. R. Micromechanics of fracture in elastomers. *J. Mater. Sci.* **19,** 3612–3619 (1984).
4. Tanaka, Y., Fukao, K., Miyamoto, Y. & Sekimoto, K. Discontinuous crack fronts of three-dimensional fractures. *Europhys. Lett.* **43,** 664–670 (1998).
5. Baumberger, T., Caroli, C., Martina, D. & Ronsin, O. Magic angles and cross-hatching instability in hydrogel fracture. *Phys. Rev. Lett.* **100,** 178303 (2008).
6. Katzav, E., Adda-Bedia, M. & Derrida, B. Fracture surfaces of heterogeneous materials: a 2D solvable model. *Europhys. Lett.* **78,** 46006 (2007).
7. Larralde, H. & Ball, R. C. The shape of slowly growing cracks. *Europhys. Lett.* **30,** 87–92 (1995).
8. Ramanathan, S., Ertas, D. & Fisher, D. S. Quasistatic crack propagation in heterogeneous media. *Phys. Rev. Lett.* **79,** 873–876 (1997).
9. Gao, H. J. & Rice, J. R. A first-order perturbation analysis of crack trapping by arrays of obstacles. *J. Appl. Mech. Trans. ASME* **56,** 828–836 (1989).
10. Freund, L. B. *Dynamic Fracture Mechanics* (Cambridge Univ. Press, 1998).
11. Goldman, T., Livne, A. & Fineberg, J. Acquisition of inertia by a moving crack. *Phys. Rev. Lett.* **104,** 114301 (2010).
12. Ponson, L., Bonamy, D. & Bouchaud, E. Two-dimensional scaling properties of experimental fracture surfaces. *Phys. Rev. Lett.* **96,** 035506 (2006).
13. Pons, A. J. & Karma, A. Helical crack-front instability in mixed-mode fracture. *Nature* **464,** 85–89 (2010).

14. Ronsin, O., Caroli, C. & Baumberger, T. Crack front echelon instability in mixed mode fracture of a strongly nonlinear elastic solid. *Europhys. Lett.* **105,** 34001 (2014).
15. Pham, K. H. & Ravi-Chandar, K. On the growth of cracks under mixed-mode I plus III loading. *Int. J. Fract.* **199,** 105–134 (2016).
16. Chen, C. H. *et al*. Crack front segmentation and facet coarsening in mixed-mode fracture. *Phys. Rev. Lett.* **115,** 265503 (2015).
17. Leblond, J.-B. & Ponson, L. Out-of-plane deviation of a mode I+III crack encountering a tougher obstacle. *C. R. Méc.* **344,** 521–531 (2016).
18. Livne, A., Cohen, G. & Fineberg, J. Universality and hysteretic dynamics in rapid fracture. *Phys. Rev. Lett.* **94,** 224301 (2005).
19. Boue, T. G., Cohen, G. & Fineberg, J. Origin of the microbranching instability in rapid cracks. *Phys. Rev. Lett.* **114,** 054301 (2015).
20. Ramanathan, S. & Fisher, D. Dynamics and instabilities of planar tensile cracks in heterogeneous media. *Phys. Rev. Lett.* **79,** 877–880 (1997).
21. Rice, J. R. 1st-order variation in elastic fields due to variation in location of a planar crack front. *J. Appl. Mech. Trans. ASME* **52,** 571–579 (1985).
22. Kolvin, I., Cohen, G. & Fineberg, J. Crack front dynamics: the interplay of singular geometry and crack instabilities. *Phys. Rev. Lett.* **114,** 175501 (2015).
23. Dalmas, D., Barthel, E. & Vandembroucq, D. Crack front pinning by design in planar heterogeneous interfaces. *J. Mech. Phys. Solids* **57,** 446–457 (2009).
24. Chopin, J., Prevost, A., Boudaoud, A. & Adda-Bedia, M. Crack front dynamics across a single heterogeneity. *Phys. Rev. Lett.* **107,** 144301 (2011).
25. Vasoya, M., Unni, A. B., Leblond, J. B., Lazarus, V. & Ponson, L. Finite size and geometrical non-linear effects during crack pinning by heterogeneities: an analytical and experimental study. *J. Mech. Phys. Solids* **89,** 211–230 (2016).
26. Adda-Bedia, M., Arias, R. E., Bouchbinder, E. & Katzav, E. Dynamic stability of crack fronts: out-of-plane corrugations. *Phys. Rev. Lett.* **110,** 014302 (2013).
27. Leblond, J. B., Karma, A. & Lazarus, V. Theoretical analysis of crack front instability in mode I+ III. *J. Mech. Phys. Solids* **59,** 1872–1887 (2011).
28. Adda-Bedia, M. Path prediction of kinked and branched cracks in plane situations. *Phys. Rev. Lett.* **93,** 185502 (2004).
29. Bouchbinder, E., Mathiesen, J. & Procaccia, I. Branching instabilities in rapid fracture: dynamics and geometry. *Phys. Rev. E* **71,** 056118 (2005).
30. Bouchbinder, E., Livne, A. & Fineberg, J. Weakly nonlinear theory of dynamic fracture. *Phys. Rev. Lett.* **101,** 264302 (2008).

Acknowledgements

J.F. and I.K. acknowledge the support of the Israel Science Foundation (grant no.1523/15), as well as the US-Israel Bi-national Science Foundation (grant no. 2016950). I.K. thanks I. Svetlizky and E. Katzav for fruitful discussions about step stability. I.K. is grateful to P. M. Chaikin for an enlightening conversation on the complexity of fracture surfaces.

Author contributions

I.K. and G.C. designed the gel preparation method and fracture experiments. I.K. synthesized the gel samples, performed the fracture experiments and surface profilometry, and analysed data. J.F. conceived the 3D crack front imaging, and initiated and supervised the research. The manuscript was written by all authors.

Additional information

Supplementary information is available in the online version of the paper. Reprints and permissions information is available online at www.nature.com/reprints. Publisher's note: Springer Nature remains neutral with regard to jurisdictional claims in published maps and institutional affiliations. Correspondence and requests for materials should be addressed to J.F.

Competing financial interests

The authors declare no competing financial interests.

Methods

Gel preparation. We prepared 14% (w/v) polyacrylamide gels crosslinked with 2.6% *N*,*N*′-Methylenebisacrylamide/acrylamide (Sigma-Aldrich). Bulk polymerization was initiated with 0.1% ammonium persulfate and catalysed with 0.05% tetramethylethylenediamine (TEMED). The solution was then poured into a home-made mould. The mould was constructed of two optically flat glass bars that are placed parallel to each other on a glass base plate. The faces of the resulting gel, which inherit the flatness and parallelity of these bars, enabled undistorted optical access through the two *xz* faces of the sample. A thin acrylic plate is fitted between the bars to act as a cover, and two machined acrylic spacers supported the cover above the base plate. During polymerization, the mould was surrounded by a 'bath' of the polymer solution. Prior to polymerization, the mould parts and bath were rinsed with soap, dried and then cleansed with ethanol. After assembling the mould, the solution was poured so as to fill the bath and submerge the mould. This technique prevents the sample from having free surfaces that can create anisotropic stresses during polymerization and destroy the optical uniformity of the gel. To prevent polymerization inhibition by atmospheric oxygen, the bath together with mould and solution were placed in a sealed container filled with argon gas. Polymerization was completed within 90 min, after which the gel sample was carefully extracted from the mould and cut to a rectangular shape of dimensions $54 \times 94 \times 4.6\,\mathrm{mm}^3$ ($x \times y \times z$).

Fracture experiments. The sample was loaded within two grips positioned at the ends of the sample's *y* dimension leaving 56 mm of free material. Fractures were initiated by two different methods. When very slow fracture was required, a small notch was imposed at the sample's edge at its mid-plane and an initial seed crack was made, using a scalpel at the notch's centre. This crack then propagated into the sample by applying opposing point loads to the notch faces until a sharp seed crack of desired length was obtained. Only then was tension applied to the sample (by displacing the grips at a rate of 50 μm s^{-1}) until slow (for example, $v = 0.005 c_R$) crack propagation initiated. A second method was used to obtain more rapid fracture. In this method, prior to fracture, we first applied a constant displacement to the sample by translating both grips anti-symmetrically so that the centre *xz* plane was stationary. A seed crack was then introduced by pushing a glass fibre of diameter 100 μm via a translation stage through the edge of the sample at its mid-plane (in *y*) until propagation initiated. Using this method, the sample was slightly overstressed prior to initiation of propagation and the more rapid velocities were obtained. In both methods, these careful crack initiation procedures were necessary to ensure that no initial surface structure was induced prior to fracture initiation. Images of the moving front were obtained by shining a beam of collimated (light-emitting diode) light through the bulk of the gel in the *y* direction. The grips had built-in optical windows that enabled collimated illumination and imaging of the fracture plane. A 270 mm lens collected the outgoing light and projected the image of the *xz* mid-plane of the sample onto the sensor of a high-speed camera (Y4-S2, IDT). We recorded images at a spatial resolution of 10 μm per pixel and at rates of 10,000–15,000 frames per second. Due to boundary effects, we had a clear view of only the centre 2 mm of the total 4.6 mm sample thickness. During crack propagation through the gel, the high curvature at the crack front deflected the incoming light. As a result crack fronts appeared as a sharply defined shadow that progressed into an otherwise uniformly illuminated frame.

Surface profilometry. Immediately following each experiment, we made a cast of the fracture surface using polyvinyl siloxane (Elite HD+, Super Light Body, Zhermack). The cast captures surface patterns in microscopic detail. This was verified by comparing height measurements of a 120 μm grid lithography etched on glass with a cast of the same grid. The surface casts were measured with an optical profilometer (Contour GT-I, Bruker) to produce 3D height maps with a lateral resolution of 2 μm and a vertical resolution of 1 μm.

Image processing. Crack fronts were extracted from shadow images at sub-pixel (~3 μm) resolution. Shadow images were divided by a background image and the front position was defined using a threshold of 0.5. To find the point where relative image intensity passed the threshold we cubically interpolated image intensity along the *x* axis, enabling our sub-pixel resolution.

Matching crack fronts and fracture surface patterns. Fracture steps produced a cusp-like deformation in the crack front. We first detected the cusp locations at each front and obtained the step-line pattern in the crack frame, which was elastically deformed relative to the material rest frame. We then extracted the contours of the step-lines in the material rest frame from the profilometric measurement. The two patterns were then superposed by imposing both a global translation and homogeneous deformation.

Measurement of the angles θ and β in Fig. 3b. Given a series of crack fronts along a step-line, we computed the local curvature by numerical differentiation (using a second-order Savitzky–Golay filter and with a window size of 5 pixels). We then detected the point of maximum curvature (which we identified as the local position of the step) and estimated the local front slope at this point. The angle β is defined as the angle between the normal to this local tangent to the front and the *x* axis.

We define a step-line as the curve traced by these positions as the crack front propagated in time. The local slope of the step-line at each point where β was determined (again using a Savitzky–Golay filter with a window size of 5 pixels) yielded the angle θ; defined as the difference between β and the angle defined by the step-line and the *x* axis. Using this procedure, we were able to determine β to an accuracy of 4°, which corresponds to the r.m.s. variation of the angle θ in Fig. 3b. The selection of θ is therefore extremely sharp; the variance in the measured values of θ essentially reflects experimental accuracy, and not systematic variations. The number of data points used to determine the range of θ for a given β was at least 10, and exceeded 50 for $-35 < \beta < 25$.

Derivation of the front shape $\delta x(z)$ from $\delta A(z)$. Consider a quasistatic straight crack front $x(z) = x_0$ which is parallel to the *z* axis and constitutes the edge of a semi-infinite tensile (Mode I) crack lying in the plane $y = 0$. As derived first by Rice[21] any small (that is, first order) in-plane perturbation to the front profile $x = x_0 + \delta x(z)$ produces a *z*-dependent stress field around the crack front $\sigma \sim K(z)/\sqrt{r}$. Here *r* is understood to be the distance from a point on the front $\mathbf{p} = (x(z), 0, z)$ to a point in the *xy* plane that intersects the front at **p**. The stress intensity factor (SIF) $K(z) = K_0 + \delta K(z)$ is composed of the unperturbed SIF K_0 and the perturbation

$$\frac{\delta K}{K_0} = -\frac{1}{2}\mathcal{H}\left[\frac{\partial \delta x}{\partial z}\right] \tag{2}$$

where $\mathcal{H}[f] = \pi^{-1}\int (\mathrm{d}z')/(z - z')f(z')$ is the Hilbert transform. Following Freund[10] the energy release rate at **p** is proportional to the SIF squared: $G \sim K^2 \sim K_0^2 + 2K_0\delta K$. On the other hand, the fracture energy is assumed to take the form $\Gamma = \Gamma_0(v)(1 + \delta A(z))$, where *v* is the local crack velocity. For the small values of *v* observed in our experiments, however, Γ_0 is practically constant. Energy balance $G = \Gamma$ therefore dictates that to the zeroth order $\Gamma_0 = G_0 \sim K_0^2$ and that to the first order in δx

$$-\mathcal{H}\left[\frac{\partial \delta x}{\partial z}\right] = \delta A(z) \tag{3}$$

To solve for the front shape, the Hilbert transform can be inverted using the identity $\mathcal{H}^2 = -1$ to obtain $\delta x(z) = \int \mathrm{d}z' \mathcal{H}[\delta A]$. Assuming that $\delta A(z) = (2H/\pi W)(1 \pm \alpha(2z/W))/(1 + (4z^2/W^2))$ we find that $\mathcal{H}[\delta A](z) = (2H/\pi W)((2z/W) \mp \alpha)/(1 + (4z^2/W^2))$. Straightforward integration then yields equation (1).

It is interesting to note that when second-order corrections to *G* due to large front perturbations[25] are taken into account, the value of $H = \int \mathrm{d}z\, \delta A$ does not change.

Estimation of W and α for isolated step-lines. We estimated *W* by numerically differentiating the crack front (using a second-order Savitzky–Golay and with a window size of 5 pixels), and measuring the distance between the two extrema that appear at the step location. For the data in Fig. 4b $W = 50^{+10}_{-3}$ μm is constant regardless of the variation of *H* (see Supplementary Fig. 1). We therefore fixed $W = 50$ μm and initially performed fits over all our data with *H* and α as free parameters. We found that the value of $\alpha = 0.24 \pm 0.08$ was uncorrelated with *H*. The value of α justifies our estimation of *W*; the analytical derivative of the functional form $\delta x(z) = cz + (H/\pi)[1/2\log(1 + (4z^2/W^2)) \pm \alpha \arctan(2z/W)]$, that is, $(\partial x(z)/\partial z) = c + (2H/\pi W)((2z/W) \pm \alpha)(1 + (4z^2/W^2))$, has extrema that are separated approximately by *W* with an error term $O(\alpha^2)$. Since $\alpha^2 \ll 1$ the numerical estimation of *W* is correct. The values of *H* in Fig. 4b were in the end obtained by fixing both α and *W* and fitting to $\delta x(z)$ with *H* as the sole free parameter. In cases where more than one step existed along the front at a given time, it was necessary to add a global quadratic term to $\delta x(z)$ to account for the long-range curvature induced by neighbouring steps.

Fits to double nucleation (for example, Fig. 2b,e). To extract the amplitude *H* in double nucleation cases, we used a superposition $\delta x(z - z_1) + \delta x(z - z_2)$, where $z = z_{1,2}$ are the locations of the two steps. As we observe that both steps grow in exactly the same way, we used the same amplitude *H* for both $\delta x(z - z_1)$ and $\delta x(z - z_2)$.

Code availability. Custom computer codes used in this work are available from the corresponding author upon request.

Data availability. The data supporting the findings of this study are available within the paper and its supplementary information files and available from the corresponding author upon reasonable request.